ACS APPLIED MATERIALS & INTERFACES

Research Article

www.acsami.org

Tailoring Crystal Structure and Morphology of $LiFePO_4$/C Cathode Materials Synthesized by Heterogeneous Growth on Nanostructured $LiFePO_4$ Seed Crystals

Dong-Wook Han,[†] Won-Hee Ryu,[†] Won-Keun Kim,[†] Sung-Jin Lim,[†] Yong-Il Kim,[‡] Ji-Yong Eom,*[,§] and Hyuk-Sang Kwon*[,†]

[†]Department of Materials Science & Engineering, Korea Advanced Institute of Science & Technology, 373-1, Guseong-dong, Yuseong-gu, Daejeon 305-701, Republic of Korea

[‡]Korea Research Institute of Standards and Science, P.O. Box 102, Yuseong-gu, Daejeon 305-340, Republic of Korea

[§]Electrochemical Engine Center (ECEC) and Departments of Materials Science and Engineering and Mechanical Engineering, The Pennsylvania State University, University Park, Pennsylvania 16802, United States

ABSTRACT: Porous and coarse (5−10 μm) $LiFePO_4$/C composites with excellent electrochemical performance were synthesized by a growth technology using nanostructured (100−200 nm) $LiFePO_4$ as seed crystals for the 2nd crystallization process. The porous and coarse $LiFePO_4$/C presented a high initial discharge capacity (~155 mA h g^{-1} at 0.1 C), superior rate-capability (~100 mA h g^{-1} at 5 C, ~65 % of the discharge capacity at 0.1 C), and excellent cycling performance (~131 mA h g^{-1}, ~98 % of its initial discharge capacity after 100 cycles at 1 C). The improvement in the rate-capability of the $LiFePO_4$/C was attributed to the high reaction area resulted from the pore tunnels formed inside $LiFePO_4$ particles and short Li-ion diffusion length. The improved cycling performance of the $LiFePO_4$/C resulted from the enhanced structural stability against Li-deficient $LiFePO_4$ phase formation after cycling by the expansion of the 1D Li-ion diffusion channel in the $LiFePO_4$ crystal structure.

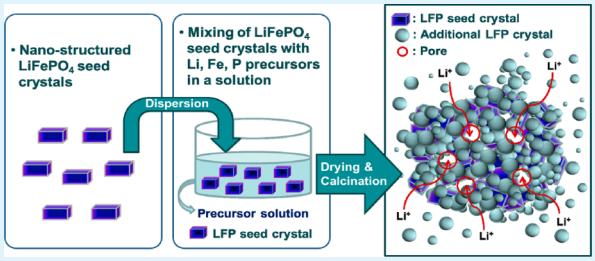

KEYWORDS: *lithium iron phosphate, porous, seed crystals, heterogeneous particle growth, lithium-ion batteries*

1. INTRODUCTION

$LiFePO_4$ with an ordered olivine structure is considered one of the most promising cathode materials for large-sized Li-ion batteries due to its excellent structural stability at elevated temperatures, high reversibility of Li-ion insertion/extraction, low cost of starting materials, and nontoxicity.[1−4] However, despite the numerous merits of $LiFePO_4$, its practical application has been limited by its inherently poor kinetic properties caused by low electronic and ionic transfer (σ_e = 10^{-1} S cm^{-1}, D_{Li+} = 10^{-14} cm^2 s^{-1} at room temperature) in the $LiFePO_4$ lattice structure.[2−6] Recently, an improvement in the kinetic properties of $LiFePO_4$ has been accomplished by carbon coating ($LiFePO_4$/C composite),[7−10] particle size reduction to the nanoscale,[11−14] and heteroatom doping.[15] However, the gravimetric/volumetric energy density of a nanostructured $LiFePO_4$ electrode is inevitably reduced because the tap density of a $LiFePO_4$ electrode decreases as the $LiFePO_4$ particle size approaches the nanoscale, and the mass fraction of bulky and inactive conducting carbons increases to secure the electrical contact between the $LiFePO_4$ nanoparticles.[16,17] Thus, it is essential to develop high-performance $LiFePO_4$/C composites with high energy density or high tap density.

To realize high power $LiFePO_4$/C composites with no expense of energy density, the following requirements must be taken into consideration: (i) the microscale size of $LiFePO_4$ particles, (ii) a large electrode/electrolyte interface area to decrease the applied current density per unit surface area, (iii) the particle morphology to reduce the Li-ion diffusion length in $LiFePO_4$ particles, and (iv) the uniform distribution of conductive carbons to increase the electronic conductivity of $LiFePO_4$.[18] Thus, porous and coarse $LiFePO_4$/C, which exists as clusters comprised of nano- or sub-microsized $LiFePO_4$ primary particles, has been suggested by several research groups.[19−22] However, unlike previous studies on the synthesis of $LiFePO_4$/C that use common synthetic routes (e.g., coprecipitation, spray pyrolysis, and the hydrothermal process), porous and coarse $LiFePO_4$/C was obtained here by a simple and novel growth technology using $LiFePO_4$ nanocrystals as seed crystals.

The schematic illustration for the formation of porous and coarse $LiFePO_4$/C, proposed in this study, is presented in Figure 1. First, nanoscale (100−200 nm) $LiFePO_4$ crystals are used as seed crystals for the 2nd crystallization process. The seed crystals are uniformly mixed with additional Li, Fe, P precursors and sucrose in a solvent, and then the collected mixed powders are heat-treated for crystallization. We

Received: November 8, 2012
Accepted: January 26, 2013
Published: January 27, 2013

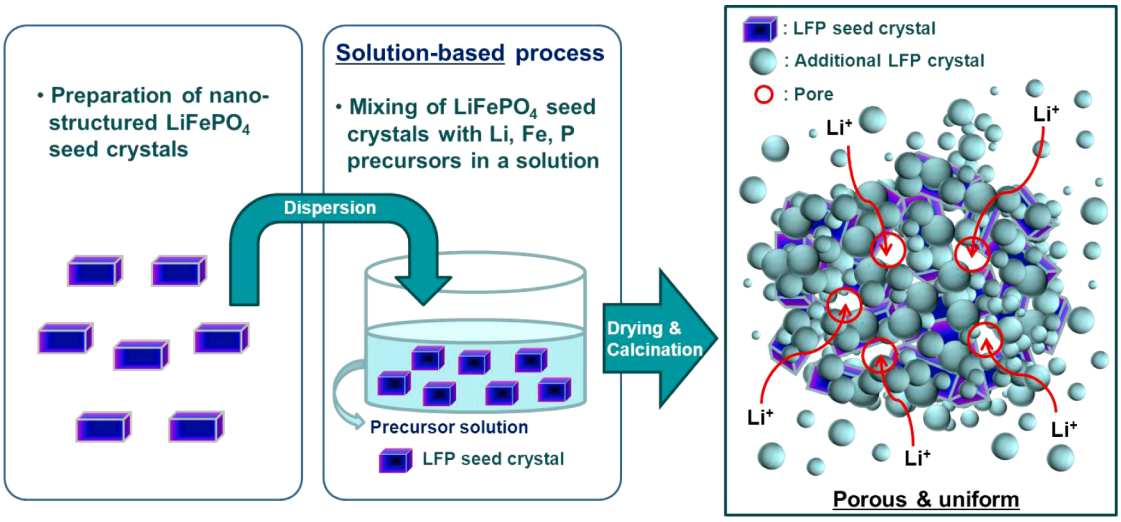

Figure 1. Schematic illustration of the growth technology using nanostructured $LiFePO_4$ seed crystals for the 2nd crystallization process proposed in this study.

anticipate that the existing $LiFePO_4$ seed crystals will act as heterogeneous nucleation sites for the 2nd crystallization of $LiFePO_4$, thereby forming uniform and coarse particles with high tap density. Further, the gas evolved from the carbonaceous reaction during the heat treatment or mismatched neighboring crystals that have grown on the seed crystals would form pore tunnels into the coarse $LiFePO_4/C$ particles, through which electrolyte may directly be in contact with the inside of the particle for improving reaction kinetics in Li-ion insertion/extraction.

Thus, the research objective of this study is to investigate the morphology and electrochemical performance of the porous and coarse $LiFePO_4/C$ composite synthesized by a growth technology using nanostructured (100−200 nm) $LiFePO_4$ as seed crystals for the 2nd crystallization process.

2. EXPERIMENTAL SECTION

2.1. Material Preparation and Characterization. Porous and coarse $LiFePO_4/C$ composites were synthesized by a growth technology using commercial nanoscale (100−200 nm) $LiFePO_4$ crystals as heterogeneous nucleation sites for the growth of $LiFePO_4$ to coarse particle clusters. The $LiFePO_4$ seed crystals were dispersed in a deionized (DI) water/ethanol mixed solution in which sucrose (3 wt % carbon) was dissolved, and then Li, Fe, P precursors ($LiNO_3$, $FeSO_4{\cdot}7H_2O$, and $NH_4H_2PO_4$) were added to the solution. The weight ratio between the seed crystals and the expected total amount of $LiFePO_4$ powder was 1:2 (w/w). The precursor mixture was stirred for 6 h with N_2 bubbling and then dried at 120 °C in a vacuum oven to prevent the oxidation of ferrous ions (Fe^{2+}) in $FeSO_4{\cdot}7H_2O$. The end product, $LiFePO_4/C$, was obtained by crystallization at 650 °C for 10 h in 5 wt % H_2 + N_2 mixed gas flow. The morphology of the $LiFePO_4$ seed crystals and $LiFePO_4/C$ was characterized by scanning electron microscopy (SEM, Philips, XL30SFEG) and transmission electron microscopy (TEM, Philips, Tecnai G2 F30 S-TWIN, 300 kV). The crystal structures of the $LiFePO_4$ seed crystals and $LiFePO_4/C$ were confirmed by X-ray powder diffraction (XRD, Rigaku D/MAX-IIIC, 3 kW) and high-resolution powder neutron diffraction (HRPD, high-resolution powder diffractometer at the Hanaro Center of the Korea Atomic Energy Research Institute), and the combined Rietveld refinements for the XRD and HRPD patterns were conducted. Herein, structural refinement cycles included zero-point shift, scale factor, lattice parameters, and background parameters as variables. Following satisfactory matching of the peak positions, the atomic positions, thermal parameters, and peak profile parameters, including the peak asymmetry, were refined. The residual carbon content in $LiFePO_4/C$ composites was measured with an element analyzer (EA, CE Instruments, EA1110-FISONS), and Brunauer-Emmett-Teller (BET) surface area and pore size/volume analysis was performed using a surface area analyzer (BET, BEL Japan Inc., BELSORP-max). To estimate the tap density of the $LiFePO_4$ seed crystals and $LiFePO_4/C$, the materials (0.75 g) were put into a measuring cylinder and tapped for 5 min.[20]

2.2. Cell Fabrication and Electrochemical Analysis. To fabricate the electrode, a mixture of 75 wt % of each active material and 17 wt % acetylene black was added to *N*-methyl-2-pyrrolidene (NMP) solvent containing 8 wt % polyvinylidene fluoride (PVdF). This slurry was pasted onto an Al foil substrate and then dried at 120 °C for 6 h in a vacuum oven. The dried paste was pressed and then punched into a disc shape with a diameter of 1.3 cm. The electrochemical properties of the prepared electrodes were evaluated using 2016 coin-type cells that were assembled in an Ar-filled glove box. Li-metal foil (Cyprus Foote Mineral, 99.98%) was used as a counter electrode, and 1 M $LiPF_6$ dissolved in 1:1 (v/v) ethylene carbonate (EC) and dimethyl carbonate (DMC) was used as the electrolyte. The charge/discharge characteristics of the fabricated cells were measured with a battery cycler (Toscat-3100u, Toyo System). For the initial two cycles, the cells were charged at a constant current density of 0.1 C until 4.3 V (vs Li^+/Li) and were continuously applied at a constant voltage of 4.3 V until a capacity of 0.05 C and then discharged at a constant current density of 0.1 C until 2.5 V. From the 3rd cycle onward, the cells were charged and discharged (0.1 C) galvanostatically between 2.5 and 4.3 V. For convenience, the discharge capacity of the materials with cycling was collected from the 3rd cycle.

3. RESULTS AND DISCUSSION

Figure 2 exhibits the scanning electron microscopy (SEM) and transmission electron microscopy (TEM) images of commercial $LiFePO_4$ seed crystals, denoted as Seed-LFP and $LiFePO_4/C$ composites prepared by a solution-based process and those formed by the growth technology using $LiFePO_4$ seed crystals, denoted as S-LFP/C and TS-LFP/C, respectively. The Seed-LFP have plate-shaped crystal with an average width of ~100 nm and a length of ~200 nm, as shown in Figure 2a,b. Figure 2c confirms that the S-LFP/C, synthesized by a solution-based process without the Seed-LFP, features irregularly shaped and coarse (~10 μm) $LiFePO_4$ particles with smooth surfaces. However, the TS-LFP/C has relatively uniform, round, and

dx.doi.org/10.1021/am302560m | ACS Appl. Mater. Interfaces 2013, 5, 1342−1347

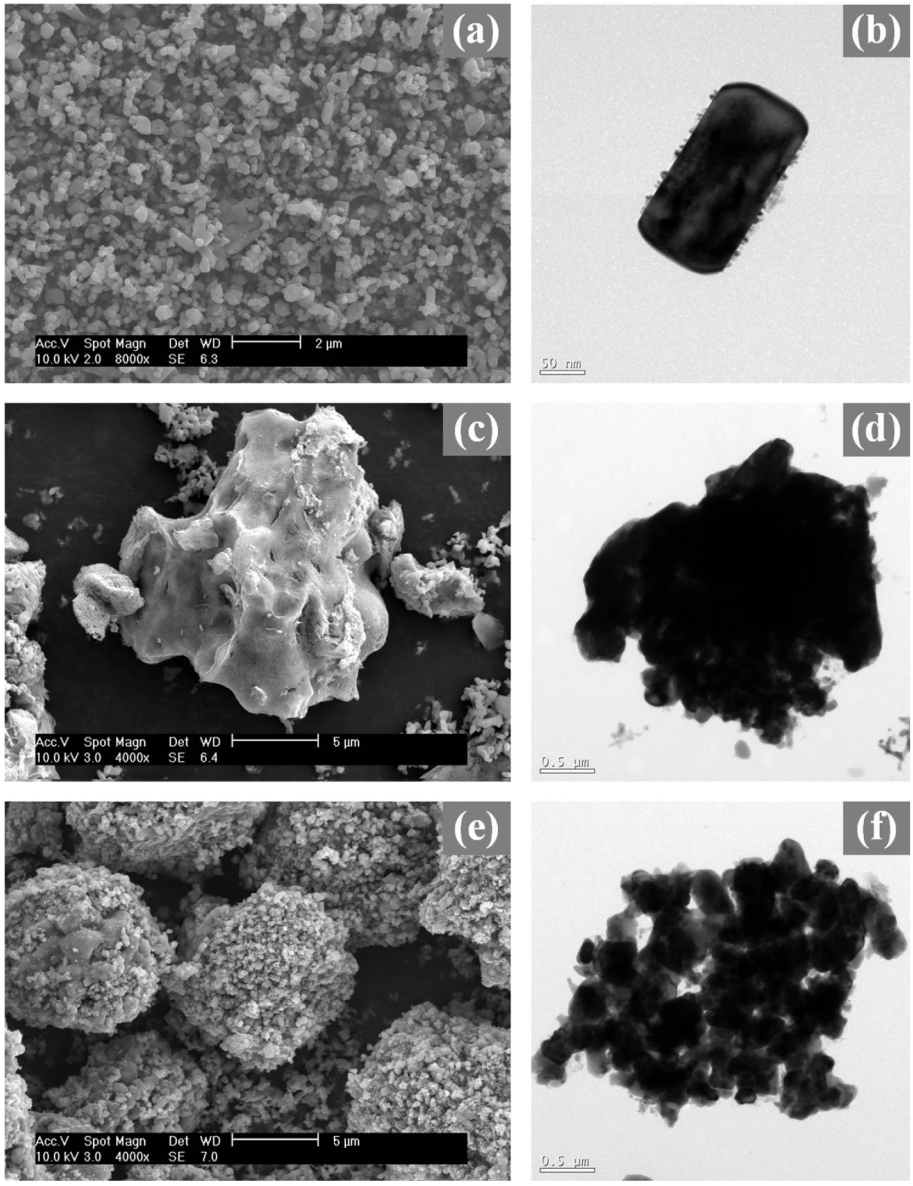

Figure 2. Scanning electron microscopy (SEM) and transmission electron microscopy (TEM) images of (a, b) Seed-LFP, (c, d) S-LFP/C, and (e, f) TS-LFP/C.

coarse (5−10 μm) $LiFePO_4$ particles, each of which comprises cluster of many $LiFePO_4$ crystals grown on the seed crystals, as shown in Figure 2e,f. Moreover, contrary to the S-LFP/C, the TS-LFP/C has a substantial number of pore tunnels inside the particle (compare parts d and f of Figure 2). The most important point here is that the morphology of the TS-LFP/C is what we anticipated in developing the porous and coarse $LiFePO_4$/C composite by the growth technology; that is, the as-prepared $LiFePO_4$ seed crystals act as heterogeneous nucleation sites with formation of pore tunnels by evolution of carbonaceous gas in the 2nd crystallization process or by the mismatch space between neighboring crystals that have grown on the seed crystals.

The X-ray powder diffraction (XRD) patterns of the three prepared materials represented in Figure 3 show that the crystalline $LiFePO_4$ seed crystals and $LiFePO_4$/C composites were synthesized without appreciable impurity phases.

The physical characteristics (residual carbon content, BET surface area, pore volume, and tap density) of the Seed-LFP, S-LFP/C, and TS-LFP/C are given in Table 1. According to the results of element analysis (EA), the amount of residual carbon in the Seed-LFP is negligible, but 2.2−2.3 wt % carbon remains in the S-LFP/C and TS-LFP/C composites. The difference between the targeted (3 wt %) and actual carbon content in $LiFePO_4$/C is due to the loss of carbons through carbothermal reactions at the $LiFePO_4$ formation temperature (650 °C).[23] The BET surface area and the average pore volume of the materials were determined from the N_2 adsorption/desorption isotherms of the particles. It is significant that in spite of the comparable actual carbon content in S-LFP/C and TS-LFP/C, the surface area (21.67 $m^2\ g^{-1}$) and pore volume (0.067 $cm^3\ g^{-1}$) of TS-LFP/C are much greater than those of S-LFP/C, which is consistent with the SEM and TEM results shown in Figure 2. The estimated tap density of the S-LFP/C and TS-LFP/C are ~0.95 g cm^{-3} and ~1.10 g cm^{-3}, respectively, which are higher than that (~0.82 g cm^{-3}) of the carbon-free nanoscale Seed-LFP. The relatively low tap density of the S-LFP/C compared with the TS-LFP/C might be attributed to

dx.doi.org/10.1021/am302560m | ACS Appl. Mater. Interfaces 2013, 5, 1342−1347

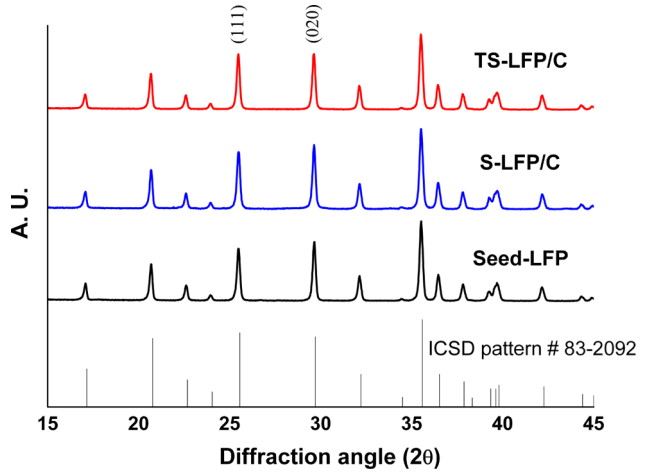

Figure 3. X-ray powder diffraction (XRD) patterns for the Seed-LFP, S-LFP/C, TS-LFP/C, and ICSD (Inorganic Crystal Structure Database) reference pattern (no. 83-2092; triphylite $LiFePO_4$) in JADE software.

Table 1. Residual Carbon Content, BET Surface Area, Pore Volume, and Tap Density of the Seed-LFP, S-LFP/C, and TS-LFP/C

samples	residual carbon content (wt %)	BET surface area (m^2 g^{-1})	pore volume (cm^3 g^{-1})	tap density (g cm^{-3})
Seed-LFP	0.0560	19.0399	0.080 115	~0.82
S-LFP/C	2.2892	7.4866	0.018 276	~0.95
TS-LFP/C	2.2113	21.6683	0.067 353	~1.10

the irregular-shaped $LiFePO_4$ particles of the S-LFP/C, as shown in Figure 2c.

Figure 4a shows the initial galvanostatic voltage profiles of the Seed-LFP, S-LFP/C, and TS-LFP/C at a rate of 0.1 C. Though the Seed-LFP has nanosized $LiFePO_4$ particles, its discharge capacity is ~110 mA h g^{-1}, which is much lower than the theoretical discharge capacity (~170 mA h g^{-1}) of $LiFePO_4$ because the electrical connection between the nanosized $LiFePO_4$ particles is not complete due to the deficiency of conducting carbons. In contrast, the compact S-LFP/C and the porous TS-LFP/C have high discharge capacities of ~153 mA h g^{-1} and ~155 mA h g^{-1}, respectively. Given that half the total weight of the TS-LFP/C originates from the Seed-LFP, the high discharge capacity of the TS-LFP/C might result from the change in the morphology and carbon content from those in the Seed-LFP as presented in Table 1.

The rate-capabilities of the Seed-LFP, S-LFP/C, and TS-LFP/C are represented in Figure 4b. The discharge capacity of the S-LFP/C achieved at low current density (0.2 C and 0.5 C) is similar to that obtained at 0.1 C. However, an abrupt decrease in the discharge capacity of the S-LFP/C is observed with an increase in the current density (>0.5 C), which indicates that Li-ion insertion/extraction into/out of the $LiFePO_4$ particles is kinetically limited at a relatively high C-rate. On the other hand, the rate-capability of the TS-LFP/C is superior to that of the S-LFP/C. At the high current density of 5 C, the discharge capacity (~100 mA h g^{-1}) of the TS-LFP/C is much higher than that of the S-LFP/C (6 mA h g^{-1}), which is attributed to the particle morphology of the TS-LFP/C characterized by the large reaction area due to its porous structure.

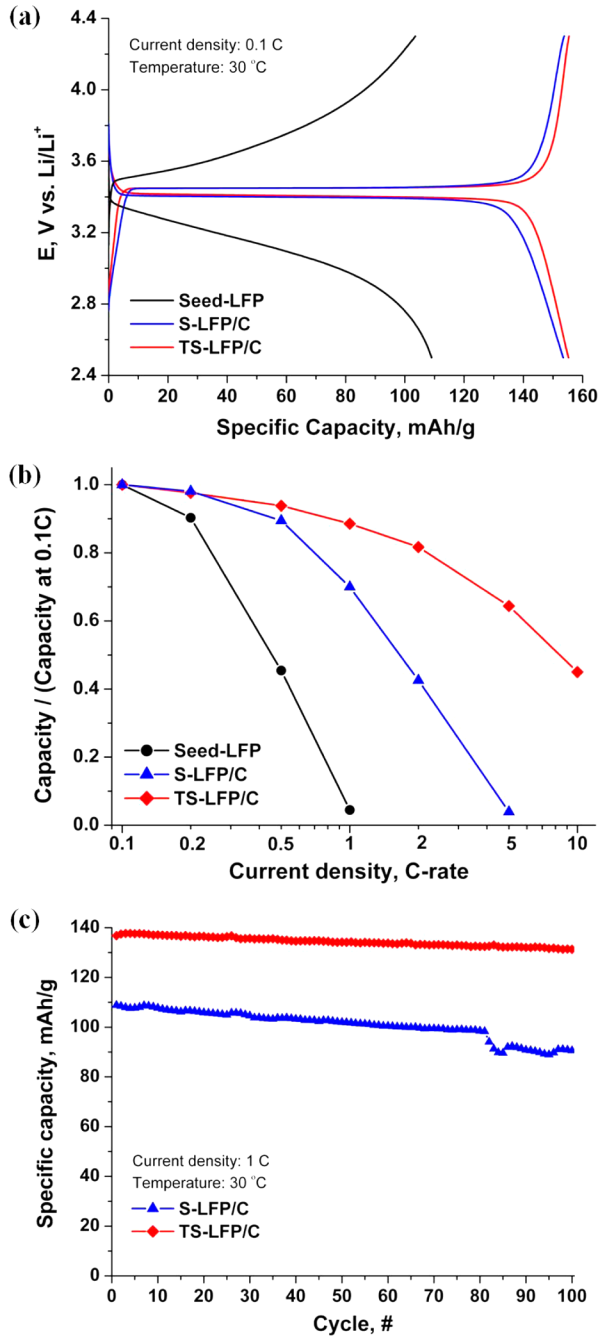

Figure 4. (a) Initial galvanostatic (0.1 C) voltage profiles, (b) rate-capability, and (c) cycling performance (1 C) of the Seed-LFP, S-LFP/C, and TS-LFP/C.

Figure 4c shows the cycling performance of the S-LFP/C and TS-LFP/C at 1 C. After 100 cycles, the TS-LFP/C exhibited a high discharge capacity of ~131 mA h g^{-1}, corresponding to ~98 % of its initial discharge capacity (~137 mA h g^{-1}), whereas the S-LFP/C showed a discharge capacity of ~90 mA h g^{-1}, ~82.6 % of its initial discharge capacity (~109 mA h g^{-1}).

Figure 5 presents the ex situ XRD patterns for the S-LFP/C and TS-LFP/C, respectively, after 100 cycles, which are compared with those in Figure 3. For the S-LFP/C electrode, its crystal structure has changed to a Li-deficient $LiFePO_4$ phase[24] as confirmed by the peaks marked in Figure 5. In contrast, the TS- LFP/C electrode sustained its pristine crystal

dx.doi.org/10.1021/am302560m | ACS Appl. Mater. Interfaces 2013, 5, 1342−1347

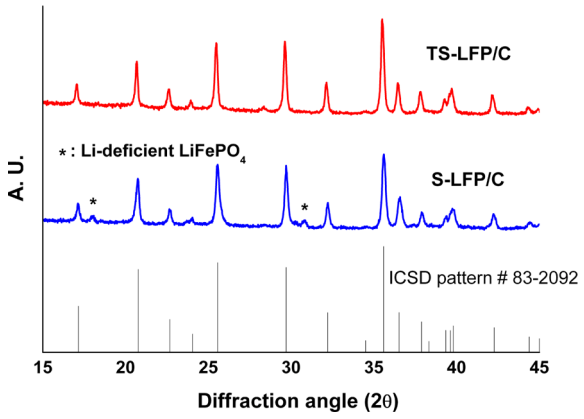

Figure 5. Ex situ X-ray diffraction (XRD) patterns for the S-LFP/C and TS-LFP/C after 100 cycles at 1 C.

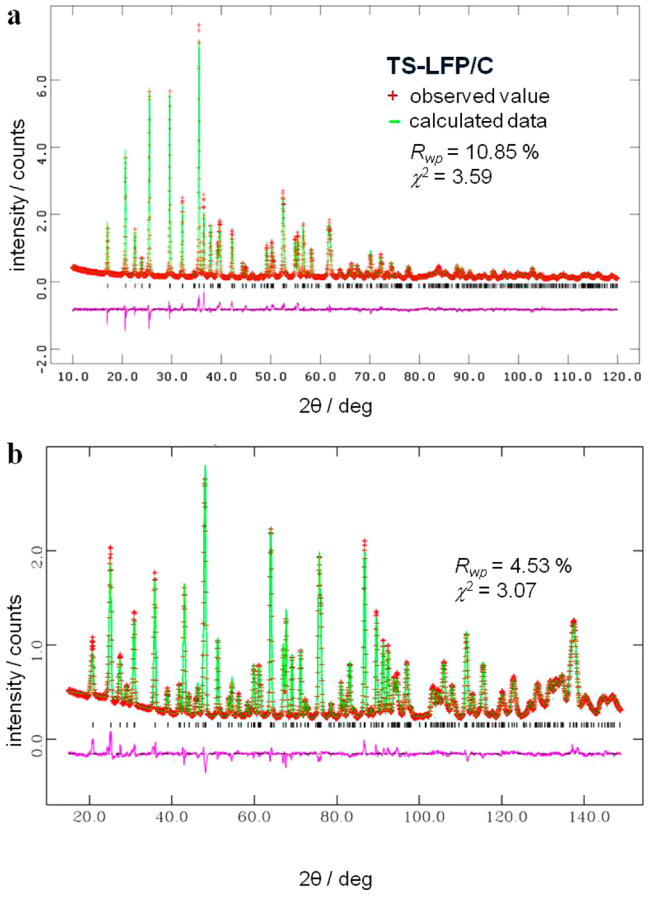

Figure 6. Combined Rietveld refinement of the (a) X-ray powder diffraction and (b) high-resolution powder neutron diffraction patterns for the TS-LFP/C.

structure. This result demonstrates that the significant capacity degradation in the S-LFP/C with cycling appears to be associated with a structural instability. From the comparison of peak intesity in the XRD patterns for the pristine S-LFP/C and TS-LFP/C shown in Figure 3, we found that the ratio of peak intensity is obviously different between the XRD patterns for the two materials, especially for the peaks that matched the (111) and (020) orientations. The discrepancy in the peak ratio may be associated with variation in the atomic positions in the $LiFePO_4$ lattice structure.[25,26]

Table 2. Lattice Parameters and Atomic Positions of the S-LFP/C and TS-LFP/C Obtained from the Combined Rietveld Refinement Results[a]

S-LFPC						
atom	site	x	y	z	g	$100 \times U_{iso}$/Å^2
Li	4a	0.0	0.0	0.0	1.0	2.28(1)
Fe	4c	0.2819(1)	0.2	0.9735(2)	1.0	0.89(2)
P	4c	0.0946(1)	0.25	0.4153(1)	1.0	0.97(1)
O	*Ac*	0.0971(2)	0.25	0.7438(1)	1.0	1.08(2)
O	4*c*	0.4574(1)	0.25	0.2075(2)	1.0	1.69(1)
O	8*d*	0.1661(1)	0.0465(1)	0.2864(2)	1.0	1.10(2)

Space group: *Pnma* (no. 62)

a = 10.3525(1), b = 6.0206(1), and c = 4.7030(1) Å, $\alpha = \beta = \gamma = 90°$

R_{wp} = 6.56 %, R_p = 4.50, χ^2 = 6.08

TS-LFP/C						
atom	site	x	y	z	g	$100 \times U_{iso}$/Å^2
Li	4a	0.0	0.0	0.0	1.0	0.78(1)
Fe	4c	0.2821(1)	0.25	0.9744(2)	1.0	0.32(2)
P	4c	0.0951(1)	0.25	0.4159(1)	1.0	0.45(1)
O	4*c*	0.0973(2)	0.25	0.7411(1)	1.0	0.32(2)
O	4*c*	0.4577(1)	0.25	0.2051(2)	1.0	0.68(1)
O	8*d*	0.1661(1)	0.0470(1)	0.2860(2)	1.0	0.36(2)

Space group: *Pnma* (no. 62)

a = 10.3489(1), b = 6.0198(7), and c = 4.7046(5) Å, $\alpha = \beta = \gamma = 90°$

R_{wp} = 6.45 %, R_p = 4.39, χ^2 = 6.98

[a]The symbols g and U_{iso} represent the occupation and isotropic thermal parameters, respectively. The numbers in parentheses are the estimated standard deviations of the last significant figure.

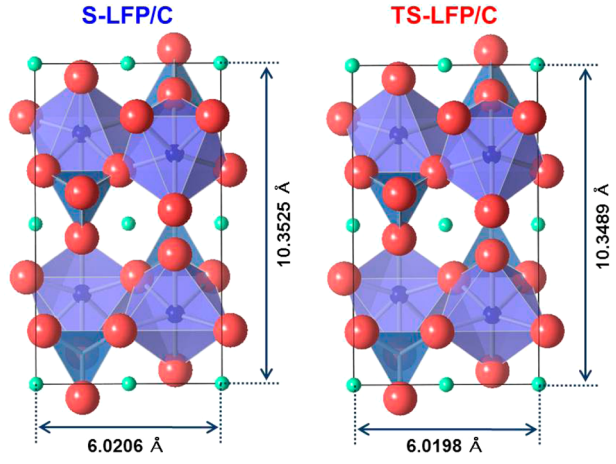

Figure 7. Visualization of (a) the $LiFePO_4$ crystal structure and (b) the unit cell structure for the S-LFP/C and TS-LFP/C.

Table 3. Unit Cell and Polyhedral (LiO_6, FeO_6, and PO_4) Volume of the S-LFP/C and TS-LFP/C

		polyhedral volume (Å^3)		
samples	unit cell volume (Å^3)	LiO_6	FeO_6	PO_4
S-LFP/C	293.13	12.4968	12.6026	1.8897
TS-LFP/C	293.09	12.5615	12.6058	1.8688

To examine this phenomenon, combined Rietveld refinements were performed for their XRD and HRPD patterns (Figure 6), and the atomic positions and the lattice parameters evaluated from the refinements are listed in Table 2. In

addition, the $LiFePO_4$ crystal structure and the unit cell structure for the S-LFP/C and TS-LFP/C are visualized using the refined structural parameters (Table 2) and VESTA program as shown in Figure 7, and the unit cell and polyhedral (LiO_6, FeO_6, and PO_4) volume of the S-LFP/C and TS-LFP/C calculated by the VESTA program is tabulated in Table 3. As a result, the LiO_6 and PO_4 polyhedral volume of the TS-LFP/C are clearly distinguished from those of the S-LFP/C, but there is not much difference in the overall unit cell volume and FeO_6 polyhedral volume between the two materials. The most interesting point here is that the TS-LFP/C with larger LiO_6 polyhedral volume compared with the S-LFP/C are structurally more stable with cycling though the PO_4 polyhedral volume of the TS-LFP/C is smaller that that of the S-LFP/C. In this regard, the minor contraction of the PO_4 polyhedra in the $LiFePO_4$ crystals may not play a crucial role in determining the structural stability of $LiFePO_4$. Thus, the presence of the Seed-LFP in the $LiFePO_4$/C synthesis process enlarges the 1D Li-ion diffusion channel in the resulting $LiFePO_4$/C, which improves the structural stability of $LiFePO_4$ after cycling.

4. CONCLUSIONS

In summary, porous and coarse (5−10 μm) $LiFePO_4$/C composites were synthesized by a simple growth technology using $LiFePO_4$ nanocrystals as seed crystals for heterogeneous nucleation. In contrast to the $LiFePO_4$/C prepared by a solution-based process, which was composed of smooth and irregular-shaped $LiFePO_4$ particles, the $LiFePO_4$/C obtained by the growth technology showed uniform, porous, and round $LiFePO_4$ particles, suggesting that the $LiFePO_4$ seed crystals served as heterogeneous nucleation sites in the 2nd crystallization process. The high initial discharge capacity and superior rate-capability of the $LiFePO_4$/C prepared by the growth technology was attributed to the high reaction area resulting from the pore tunnels formed inside $LiFePO_4$ particles and short Li-ion diffusion length. Further, the improved cycling performance of the $LiFePO_4$/C resulted from the enhanced structural stability against Li-deficient $LiFePO_4$ phase formation after cycling by the expansion of the 1D Li-ion diffusion channel in the $LiFePO_4$ crystal structure.

AUTHOR INFORMATION

Corresponding Author

*Ji-Yong Eom: phone, +1-814-863-0749; fax, +1-814-863-4848; e-mail, jyeom74@gmail.com. Hyuk-Sang Kwon: phone, +82-42-350-3326; fax, +82-42-350-3310; e-mail, hskwon@kaist.ac.kr

Notes

The authors declare no competing financial interest.

ACKNOWLEDGMENTS

This research was supported by the Basic Science Research Program through the National Research Foundation of Korea (NRF), which is funded by the Ministry of Education, Science and Technology (Grant NRF-2010-0024752) and partially funded by the BK21 Program of the Korea Ministry of Knowledge Economy.

REFERENCES

(1) Padhi, A. K.; Nanjundaswamy, K. S.; Goodenough, J. B. *J. Electrochem. Soc.* **1997**, *144*, 1188−1194.
(2) Wang, Y.; He, P.; Zhou, H. *Energy Environ. Sci.* **2011**, *4*, 805−817.
(3) Yuan, L. X.; Wang, Z. H.; Zhang, W. X.; Hu, X. L.; Chen, J. T.; Huang, Y. H.; Goodenough, J. B. *Energy Environ. Sci.* **2011**, *4*, 269−284.
(4) Yang, Z.; Zhang, J.; Lu, X.; Choi, D. *Chem. Rev.* **2011**, *111*, 3577−3613.
(5) Chung, S. Y.; Chiang, Y. M. *Electrochem. Solid-State Lett.* **2003**, *6*, A278−A281.
(6) Prosini, P. P.; Carewska, M.; Scaccia, S.; Wisniewski, P.; Pasquali, M. *Electrochim. Acta* **2003**, *48*, 4205−4211.
(7) Chen, Z.; Dahn, J. R. *J. Electrochem. Soc.* **2002**, *149*, A1184−A1189.
(8) Ravet, N.; Chouinard, Y.; Magnan, J. F.; Besner, S.; Gauthier, M.; Armand, M. *J. Power Sources* **2001**, *97-98*, 503−507.
(9) Gabrisch, H.; Wilcox, J. D.; Doeff, M. M. *Electrochem. Solid-State Lett.* **2006**, *9*, A360−A363.
(10) Herle, P. S.; Ellis, B.; Coombs, N.; Nazar, L. F. *Nat. Mater.* **2004**, *3*, 147−152.
(11) Lee, M. H.; Kim, J. Y.; Song, H. K. *Chem. Commun.* **2010**, *46*, 6795−6797.
(12) Wu, X. L.; Jiang, L. Y.; Cao, F. F.; Guo, Y. G.; Wan, L. J. *Adv. Mater.* **2009**, *21*, 2710−2714.
(13) Bueno, P. R.; Leite, E. R. *J. Phys. Chem. B* **2003**, *107*, 8868−8877.
(14) Choi, D.; Kumta, P. *J. Power Sources* **2007**, *163*, 1064−1069.
(15) Liu, H.; Cao, Q.; Fu, L. J.; Li, C.; Wu, Y. P.; Wu, H.Q. *Electrochem. Commun.* **2006**, *8*, 1553−1557.
(16) Whittingham, M. S. *Dalton Trans.* **2008**, 5424−5431.
(17) Bruce, P. G.; Scrosati, B.; Tarascon, J.-M. *Angew. Chem., Int. Ed.* **2008**, *47*, 2930−2946.
(18) Whittingham, M. S. *Chem. Rev.* **2004**, *104*, 4271−4301.
(19) Liu, J.; Conry, T. E.; Song, X.; Doeff, M. M.; Richardson, T. J. *Energy Environ. Sci.* **2011**, *4*, 885−888.
(20) Qian, J.; Zhou, M.; Cao, Y.; Ai, X.; Yang, H. *J. Phys. Chem. C* **2010**, *114*, 3477−3482.
(21) Oh, S. W.; Myung, S. T.; Bang, H. J.; Yoon, C. S.; Amine, K.; Sun, Y. K. *Electrochem. Solid-State Lett.* **2009**, *12*, A181−A185.
(22) Huang, B.; Zheng, X.; Jia, D.; Lu, M. *Electrochim. Acta* **2010**, *55*, 1227−1231.
(23) Huang, Y.-H.; Goodenough, J. B. *Chem. Mater.* **2008**, *20*, 7237−7241.
(24) Shin, H. C.; Chung, K. Y.; Min, W. S.; Byun, D. J.; Jang, H.; Cho, B. W. *Electrochem. Commun.* **2008**, *10*, 536−540.
(25) Song, M. S.; Kim, D. Y.; Kang, Y. M.; Kim, Y. I.; Lee, J. Y.; Kwon, H. S. *J. Power Sources* **2008**, *180*, 546−552.
(26) Cullity, B. D. *Elements of X-ray Diffraction*, 2nd ed.; Addison-Wesley: Boston, MA, 1978; pp 324−349.